

Porous Au–Ag Nanoparticles from Galvanic Replacement Applied as Single-Particle SERS Probe for Quantitative Monitoring

Lu Wang, Sergiy Patskovsky, Bastien Gauthier-Soumis, and Michel Meunier*

Plasmonic nanostructures have raised the interest of biomedical applications of surface-enhanced Raman scattering (SERS). To improve the enhancement and produce sensitive SERS probes, porous Au–Ag alloy nanoparticles (NPs) are synthesized by dealloying Au–Ag alloy NP-precursors with Au or Ag core in aqueous colloidal environment through galvanic replacement reaction. The novel designed core–shell Au–Ag alloy NP-precursors facilitate controllable synthesis of porous nanostructure, and dealloying degree during the reaction has significant effect on structural and spectral properties of dealloyed porous NPs. Narrow-dispersed dealloyed NPs are obtained using NPs of Au/Ag ratio from 10/90 to 40/60 with Au and Ag core to produce solid core@porous shell and porous nanoshells, having rough surface, hollowness, and porosity around 30–60%. The clean nanostructure from colloidal synthesis exhibits a redshifted plasmon peak up to near-infrared region, and the large accessible surface induces highly localized surface plasmon resonance and generates robust SERS activity. Thus, the porous NPs produce intensely enhanced Raman signal up to 68-fold higher than 100 nm AuNP enhancement at single-particle level, and the estimated Raman enhancement around 7800, showing the potential for highly sensitive SERS probes. The single-particle SERS probes are effectively demonstrated in quantitative monitoring of anticancer drug Doxorubicin release.

effect.^[2] Especially, the porous plasmonic NPs present significant larger tunability in terms of porosity, composition, and larger specific surface area and higher hot spots density compared to the nonporous nanostructures.^[3] As their plasmonic peaks can be tuned in the biological transparent window located in NIR region, the porous NPs may be implemented efficiently in biomedical applications, including bioimaging, biodetection, and drug delivery, as well as the surface-enhanced Raman scattering (SERS) based applications.^[4]

For biosensing and diagnostics, SERS sensing probes are outstanding among various methods.^[5] By highly enhancing “finger-print” Raman signal, SERS substrates and probes show promises in analytical chemistry and biochemistry detection with low detection limits.^[6] The growing demand for accurate, personalized diagnosis and therapy is opening up new areas of biomedical application with SERS individual nanoprobe,^[7] such as, multiplex Raman cellular detection and differentiation, or ultrasensitive multiplex quantitation of microorganisms.^[8]


In addition, single NPs exhibit great potential in the use of SERS nanoprobe for cyto- and histopathological diagnostics, where they can give an improvement over the existing tissue imaging system using Raman spectroscopy,^[9] by providing local enhancement in spatial Raman mapping studies at the cellular and subcellular level.^[10] Plasmonic NPs, especially Au–Ag NPs, provides adjustable SERS probes with high enhancement, due to their LSPR behaviors and their designable structures with high hot spots density. The rough surface, assemblies, nanoscale curvature and gap are promising structures for SERS.^[11] However, the reproducibility and the stability remain as the main challenge for practical applications. Therefore, it becomes important to have a controllable synthetic strategy for plasmonic NPs with designed nanostructure, clean surface and aqueous dispersibility, to facilitate the wide application in biosensing.

Porous and hollow plasmonic structures have been widely explored using the galvanic replacement reaction (GRR) approach, which removes the less noble metal from the template and replaces it with more noble metal via redox process, while forming vacancies in the multimetallic structure.^[12] In

1. Introduction

Plasmonic nanoparticles (NPs) have been strongly considered in biomedical applications, due to their adjustable localized surface plasmon resonance (LSPR) properties.^[1] Various structured plasmonic NPs have been explored due to the strong structural dependence of their optical properties. Hollow and porous NPs are promising as multifunctional platform in therapeutics owing to their unique structure with interior vacancies, and their distinctive optical properties, including the LSPR in visible-near infrared (NIR) region, and surface enhancement

L. Wang, S. Patskovsky, B. Gauthier-Soumis, M. Meunier
Laser Processing and Plasmonics Laboratory
Department of Engineering Physics
Polytechnique Montréal
C.P. 6079, Succ. Centre-ville, Montréal, Québec H3C 3A7, Canada
E-mail: michel.meunier@polymtl.ca

 The ORCID identification number(s) for the author(s) of this article can be found under <https://doi.org/10.1002/sml.202105209>.

DOI: 10.1002/sml.202105209

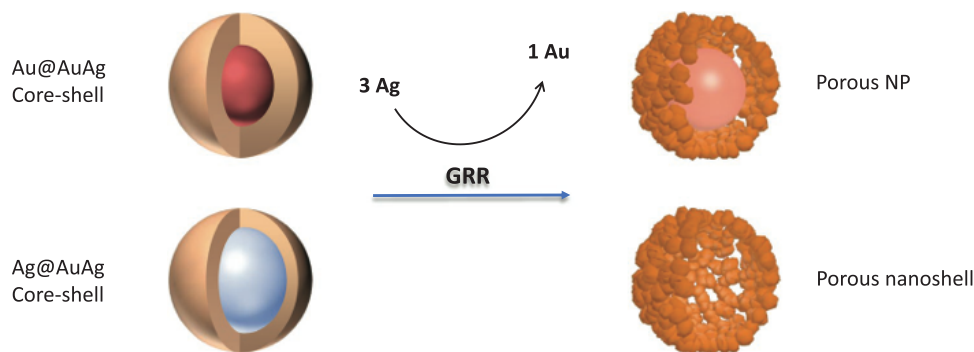


Figure 1. Galvanic replacement reaction on Au@Au/Ag and Ag@Au/Ag, resulting in porous shell with solid core (porous NP) or hollow interior (porous nanoshell), respectively.

nanostructures synthesized through GRR, Ag provides the most common sacrificial templates with its high reactivity, while porous structure and surface area are still difficult to control due to the nature of GRR for the fast reaction at the surface with dealloying reagents.^[13] Recently, some efforts were made by tailoring the GRR or partially inhibiting GRR to achieve a better controlled of voids number or spherically clustered nanostructures.^[4b,14] However, these approaches require a polymer coating during the dealloying process, which occupies the surface, and will significantly impair the access of cargo or analytes for further applications. Another way to get porous structure is to apply a strong acid to alloyed template, thus removing the sacrificial part thoroughly.^[15] For example, the concentrated nitric acid, with much stronger dealloying ability than GRR, were used for dealloying the immobilized alloy arrays. However, this stabilizing and solid phase method limit the translation toward a scalable production. To tackle the difficult stabilization, and ensure the surface accessibility in colloidal synthesis, Gao's group employed a thin hollow shell of silica using a quite elaborated process to stabilize the NPs, and finally achieved porous Au–Ag with high surface accessibility.^[4c]

Instead of regulating GRR through an external environment and the use of organic coatings, we propose to control the final structure through carefully designing the composition of the Au–Ag NP-precursors in GRR. Indeed, as the kinetics of dealloying strongly depends on the relative Ag–Au composition, we used our newly introduced combined seeded-growth and core-reduction synthesis approach to fabricate Au–Ag alloy NP-precursors with a fine control of both composition within 7% and size over 30 to 150 nm within 15%.^[16]

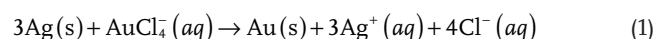
In this paper, we report a newly facile colloidal synthesis approach for porous Au–Ag NPs, which exhibit tunable optical properties, excellent drug loading capacity and ultrahigh SERS activity, providing single-particle level SERS detector for drug release. The GRR dealloying process is controlled by designing the composition, size and structure of the NP-precursors. We employed our newly Au-core and Ag-core alloy-shell NPs as precursor for the GRR dealloying, and synthesized the narrow-dispersed NPs, coefficient of deviation less than 15%, of solid core@porous shell and porous nanoshells with hollow interior. The spectral and structural evolution during dealloying and the compositional effect has been studied in detail both in

colloidal solutions and on single NPs. By controlling both the core and shell size and composition, the Au–Ag alloy core–shell NP-precursors offer a great variation and easy control of final colloidal porous structures. Well-controlled synthesis approach enables to finely tune the nanostructure, as well as their plasmonic features, including tunable redshift of plasmon peak up to NIR region, and high-density hot spots for SERS. Thanks to the polymer-free colloidal synthesis, the NPs keep a relatively large accessible surface for SERS. Single-particle level detection is demonstrated based on the strong SERS activity to provide quantitative monitoring of drug release.

2. Results and Discussion

2.1. GRR Dealloying of Au–Ag Alloy Nanoparticles

Taking advantage of the different reactivity between Au and Ag, GRR was employed to remove Ag from Au–Ag alloy. **Figure 1** illustrates that Au–Ag alloy NPs with Au and Ag cores have been used as NP-precursors, and form porous NPs with solid core (porous NPs) and with a hollow interior (porous nanoshells), respectively. These core–shell structured NP-precursors are denoted as Au@Au/Ag and Ag@Au/Ag NPs respectively and were first synthesized using our previously published seeded-growth method.^[16] The alloy shell can be adjusted freely in terms of thickness and composition, while maintaining the monodispersity of alloy NPs. Then, HAuCl₄ is applied for the GRR, and the dealloying process follows the chemical overall reaction



where the reduction potential over standard hydrogen electrode (SHE) of AuCl₄[−]/Au (0.99 V vs SHE) is higher than the one of AgCl/Ag (0.22 V vs SHE),^[17] so that each three Ag atoms are replaced by one Au atom, introducing vacancies. Combined with the concurrent Kirkendall effect, driven by the different diffusion rates between Au and Ag, GRR forms porous and hollow structure in NPs.^[4a,b,13a,18] After dealloying, Au@Au/Ag NPs transform to solid core@porous shell nanostructures with rough surface, while Ag@Au/Ag NP becomes porous shell with hollow interior as shown in Figure 1.

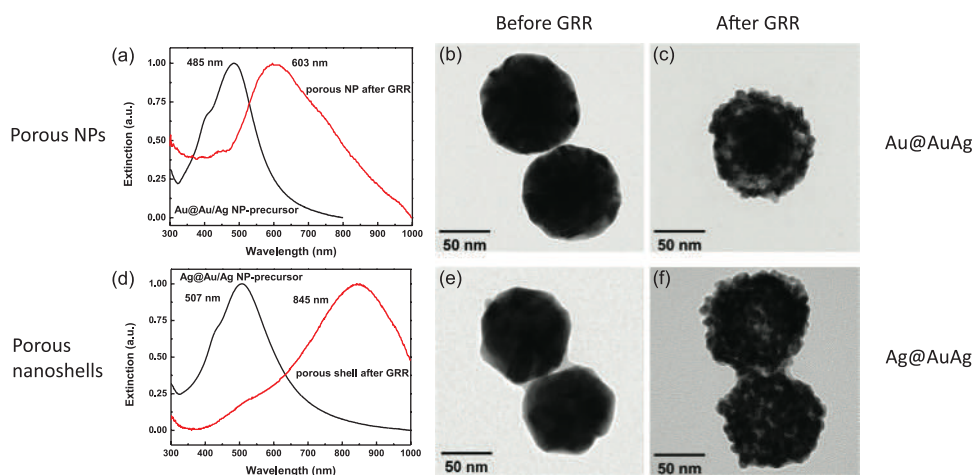


Figure 2. Typical extinction spectra a,d) and TEM images of Au@Au/Ag and Ag@Au/Ag before b,e) and after GRR c,f).

During GRR dealloying, as HAuCl_4 is slowly added into the aqueous dispersion at room temperature, the NPs colloidal color changes with time and its intensity decreases. To illustrate the optical and structural changes during dealloying of alloy NPs, two representative examples of the UV-vis spectra and transmission electron microscopy (TEM) of Au@Au/Ag and Ag@Au/Ag are shown in Figure 2. The NP-precursors are comprised of the same shell composition of Au/Ag 25/75, having respectively a 40 nm Au core and a 60 nm Ag core. After the GRR dealloying, the two types of precursors result in distinguishable spectra and structures. Plasmonic extinction peak of both types of NPs has red-shifted after GRR, by ≈ 118 nm for Au-core precursors (Figure 2a) and by ≈ 337 nm for Ag core (Figure 2d). The large optical shifts result in an obvious color change for colloidal and single NPs, the peak of hollow nanoshells even reaches NIR region, which is interesting for biomedical applications. Meanwhile, the extinction spectra broaden with the intensity decreasing, due to the porous and hollow structure, probably introducing significant phase-retardation effects.^[19] During the dealloying, spherical NPs stay relatively monodispersed while generating nanoscale rough surface and porous structure, as well as creating hollow space in the NPs. The diameter of NPs slightly increases, by $<10\%$, contrary to the shrinkage in dealloying with strong acid for fixed NPs.^[20] Au@Au/Ag NPs transform from solid spheres to porous NPs with a rough surface and many nanoscale pits near the surface (TEM shown in Figure 2b,c). Note that the Ag in the shell has been partially removed, while the Au-rich core still remains. However, Ag@Au/Ag NPs reconstruct from solid spheres to porous shells with a hollow interior (Figure 2e,f), through removing the Ag core. Therefore, for both structures, accessible surface and loading space increase remarkably and the rough surface creates local curvature, generating a high density of hot spots. Generally, the high surface energy limits the production of controllable and stable nanostructures which requires surface coating, based on the work of Dey and co-workers by hyperbranched polymer.^[21] However, by using our monodispersed alloy precursors and by adjusting the concentration of NPs and the addition rate of dealloying reagent HAuCl_4 , we can easily obtain through coating-free synthesis, well dispersed final colloidal porous nanostructures with high reproducibility.

Many details of the dealloying effect on Au–Ag alloy NPs are revealed by the high-angle annular dark field (HAADF) and energy dispersive X-ray spectroscopy (EDS) mapping under scanning transmission electron microscopy (STEM) (Figure 3). For the porous NPs dealloyed from Au@Au/Ag NP-precursors (Figure 3a–d), HAADF-STEM shows that the core remains, while large pores appear in the shell as well as a gap between the surface and core. The EDS mapping exhibits that Au accumulates near the center and at some small islands near the surface (indicated by white arrows in Figure 3a), and for Ag, there is an evident loss in the shell, while a significant part of Ag migrates to the core and remains after dealloying. It is reasonable that Ag atoms near the surface are easier to be selectively removed, while remaining Au atoms, along with newly grown ones that gather near the forefront, especially around the pores near the surface. The line profile of Au and Ag intensities demonstrate that the Au and Ag are quite equally mixed, indicating that the Au and Ag realloy during the dealloying to remain thermodynamically stable.^[22]

For porous nanoshells dealloyed from Ag@alloy NPs, we can clearly see the tangled ligaments near the surface from HAADF-STEM image (Figure 3e), and the hollow interior from the contrast between core and shell, which are created by removing large portion of the precursor, especially the Ag core. The elemental mapping and line profiles (Figure 3f–h) illustrate the shell structure and the homogeneous mixing of Au and Ag. Massive dealloying, especially dealloying from the core requires large interaction between the internal and external environment. The decrease near the center of the nanoshell in the line profile is a clear signature of the empty core and is in agreement with a simple geometry model of a transmission path through a shell structure shown in Figure S1 (Supporting Information). Due to the abundant exchange in dealloying, Au and Ag are homogeneously distributed in the nanoshell, as shown in elemental mapping and line profile (Figure 3f–h). With different diffusion rate between Au and Ag, Kirkendall effect introduced more porous structure in the shell.^[18]

By finely control the GRR reaction, even if a significant amount of Ag atoms is removed, we observed that the Au rich structure remains, preventing the collapse the final structure,

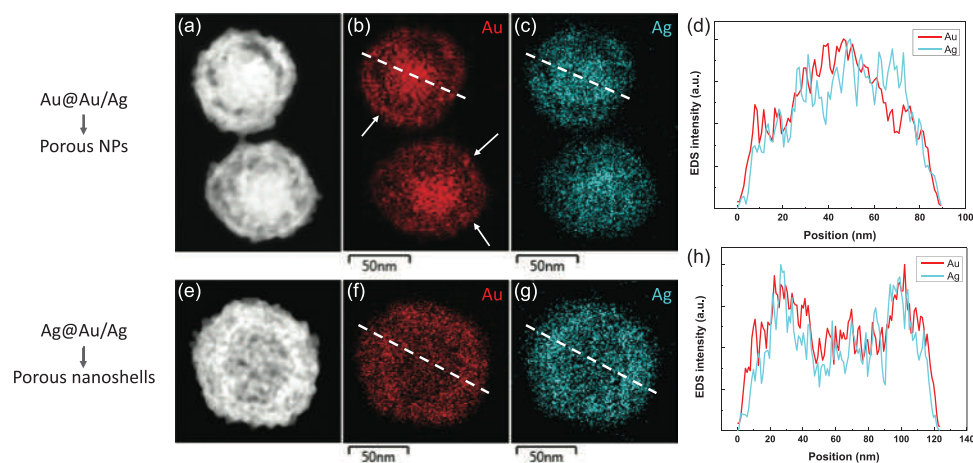


Figure 3. High-angle annular dark-field scanning transmission electron microscopy (HAADF-STEM) image of dealloyed NPs from a) Au@Au/Ag, e) Ag@Au/Ag NPs, and their respective b, c and f, g) elemental mapping of Au and Ag. Elemental composition profile along the dashed lines (in (b), (c), (f), and (g)) are shown in (d) and (h).

and that the newly attached Au atoms on the surface slightly enlarges the diameter of final NPs. The removal of Ag and atomic diffusion during the dealloying create high curvature near the surface, pits and a gap between core and shell, as well as a hollow interior. Both Au@alloy and Ag@alloy NPs become porous after dealloying, generating large accessible surface area, loading space, and high density of hot spots.

2.2. Calculation of Porosity

The porosity in final NPs can be estimated from the Au and Ag composition and size of both precursor and porous NPs and the fact that the loss of each three Ag atoms is replaced by one Au atom. The vacancy $2x$ is given by

$$\frac{Au + x}{Ag - 3x} = \frac{Au'}{Ag'} \quad (2)$$

where Au and Ag are the respective atomic percentage of Au and Ag in precursor, while Au' and Ag' are their atomic percentage in final dealloyed NPs. The removed Ag atoms and newly deposited Au atoms are quantified as $3x$ and x , respectively. Therefore, vacancy resulted from the loss of atoms is estimated as $2x$ in atomic percentage of NP-precursors. Due to the similar crystal structure and lattice constant of Au and Ag, 4.078 Å (Au) and 4.086 Å (Ag), we roughly consider the volume percentages as atomic ones. Besides the vacancy, Kirkendall effect during the mass transportation and accumulation of Au atoms on the surface, slightly enlarges the diameter, thus the volume of NPs. The volume enlargement (ΔV) is calculated through the diameter measured from TEM images

$$\Delta V = V' - V = \frac{1}{6}\pi(D'^3 - D^3) \quad (3)$$

where D and D' are the respective measured diameter of NPs before and after dealloying, as shown in Figure S2a (Supporting Information), taken from the average diameter of over fifty NPs

from TEM images. Therefore, both the vacancy generated in GRR and volume enlargement contribute to the pore structure of the NPs. If the porosity is uniformly distributed in the whole NP, porosity equals to the percentage of pore structure in the volume of final NP, as Equation (4). While in most cases, pore structure distributes in the shell, which plays the most important role in interacting with the electrolyte environment or being applied for the surface properties. Therefore, when the NPs contains a solid core (with diameter of D_{core}), we consider the pore structure distributes in the shell (with diameter of D_{shell}), as shown in Figure S2b (Supporting Information), and porosity in shell is expressed as Equation (5)

$$\text{porosity} = \frac{2xV + \Delta V}{V'} = 1 - (1 - 2x)\frac{V}{V'} = 1 - (1 - 2x)\frac{D^3}{D'^3} \quad (4)$$

Or

$$\text{porosity in shell} = \frac{2xV + \Delta V}{V_{shell}} = \frac{D_{shell}^3 - (1 - 2x)D_{core}^3}{D_{shell}^3 - D_{core}^3} \quad (5)$$

2.3. Effect of the Dealloying Degree

As dealloying reagent in GRR, the amount of HAuCl_4 has significant impact on the dealloying process. We define the term dealloying degree (d_D) to describe the amount of the added HAuCl_4 compared to Ag atoms in precursor NPs. When the ratio of added HAuCl_4 and Ag in precursors is exactly 3:1, equal to the stoichiometric ratio between $[\text{AuCl}_4]^-$ in the solution and the total number of Ag atoms in all NPs precursors in GRR, the d_D is defined as 1.0; when more HAuCl_4 added, d_D is higher than 1.0, otherwise, lower than 1.0. Thus, the equation is

$$d_D = [\text{AuCl}_4]^- / 3[\text{Ag}] \quad (6)$$

Dealloying degree describes the experimental condition in terms of how much dealloying reagent is added, but it does not reflect the detailed reaction, considering that the composition

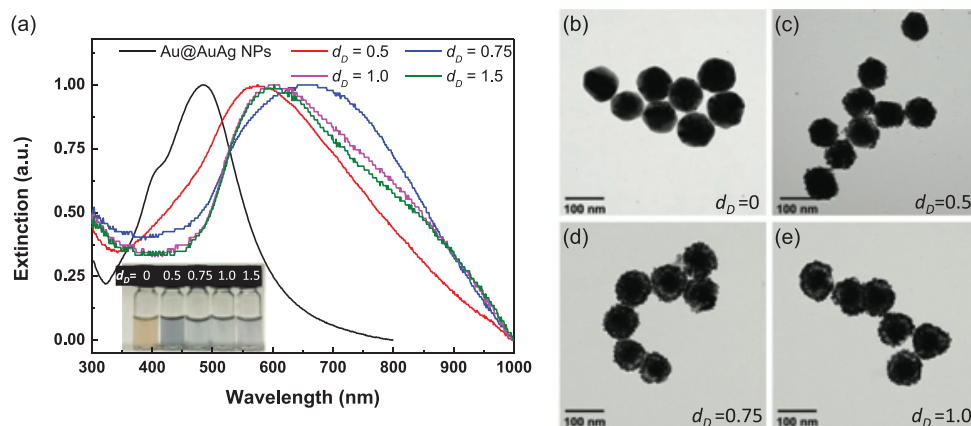


Figure 4. Effect of dealloying degree on the synthesis of porous NPs. a) Extinction spectra and b–e) TEM image of Au@Au/Ag 10/90 NP-precursor ($d_D = 0$) and porous NPs after GRR with dealloying degree (d_D) of 0.5, 0.75, and 1.0, respectively.

threshold may prevent complete dealloying, left with surplus H₂AuCl₄. The color change happens with the slow addition of H₂AuCl₄ into the precursor NP dispersions, which directly reflects the influence from the amount of added H₂AuCl₄.

To study the influence of d_D , over a fix time of 30 min at room temperature, we dealloyed Au@Au/Ag 10/90 core–shell NPs (Au@Au/Ag NPs, constituted with 40 nm core and Au/Ag 10/90 alloy shell), at $d_D = 0.5, 0.75, 1.0,$ and 1.5 . We investigated the structural features changing with d_D through TEM and UV–vis spectrophotometer characterization as well as EDS. **Figure 4** shows distinguishable spectral and structural changes from precursor to final NPs of different d_D . During the dealloying, the color of NP dispersion changes abruptly from orange to blue and gray, shown in the inserted color image in **Figure 4a**. After GRR, extinction peaks show great redshift (≈ 170 nm) and obvious broaden at lower d_D , and the redshift decreases with higher d_D , stabilizing after $d_D > 1.0$ (**Figure 4a**), showing ≈ 110 nm redshift compared to the precursor. The formation of gap and heterogeneous structure between core and shell induce broaden or even diverging of the peak. Moreover, the red-NIR spectral region (700–900 nm) is a signature of the presence of a thin Au-rich layer on the surface which is more pronounced at lower d_D of 0.75 and significantly decrease with higher d_D because of the arrangement of atoms contributing to more homogeneous composition.^[22]

Porous nanoparticles with $d_D = 0.5$ (**Figure 4c**) show mainly rough surface, and some particles begin to form the gap between core and shell, while with $d_D \geq 0.75$ (**Figure 4d,e**), NPs exhibit obvious gap between core and shell, showing similar yolk-porous shell structure. The uniformity of porous structure has been proved with low-resolution TEM images containing more porous NPs (**Figure S3**, Supporting Information). Based on the statistics from TEM images (**Table S1**, Supporting Information), we found that the core shrinks with increasing d_D . From d_D of 0.75–1.0, the core size stays relatively constant while the shell keeps enlarging, indicating that the dealloying process is concentrated in the shell. After the dealloying of shell, further dealloying deepens into the core at higher $d_D = 1.5$, as the core size decreases abruptly from ≈ 58 nm to ≈ 49 nm, while the exterior diameter of NPs stays constant compared to $d_D = 1.0$. This

can be explained by the collapse of microstructure resulting from the coalescing, which balances with further deposition of Au. In brief, dealloying near the surface begins at lower d_D , inducing yolk-porous shell structure, and more sufficient reagents drives the dealloying approaching the core. **Figure S4** (Supporting Information) shows the results from Au@Au/Ag 27/75 for d_D in the range of 0.25–1.5, and the spectral shift exhibits similar trend with **Figure 4a**, and the TEM show clear rough surface when $d_D \geq 0.5$.

As discussed with STEM results, dealloying occurs first near the surface and the Ag-rich (90 at%) shell induced violent dealloying. The dealloying induces large vacancies while the inertness of left Au and Au-rich core hinder the dealloying into the core. Therefore, the gap between the core and the shell forms. The realloying taking place during the dealloying allows GRR to penetrate inside the NPs with higher d_D . While due to the inertness of Au core, the center of the nanostructure stays intact. The gap and porous shell induces large redshift and the thin shell creates stronger electron-surface scattering effect, generating much wider plasmonic peak.^[23]

Based on the statistics of the measured core and shell size, combined with compositional results from the NPs, we calculated the overall porosity and shell porosity (**Figure 5**). With increasing d_D , more Ag gets replaced by Au, and Au fraction reaches 52% at $d_D = 1.5$ from 16% in the NP-precursor. From NP-precursor to $d_D = 0.75$, the Au composition shows a significant increase, indicating main dealloying reaction occurs at the early stage. After that, when d_D increases, the composition change is limited, especially after $d_D = 1.0$. Considering the Au core in the precursor, combined with the compositional threshold, it is difficult to have further dealloying. The overall porosity exhibits a similar trend as the Au composition of the NPs, while the shell porosity is influenced significantly by the size of the core and shell. Therefore, the shell porosity peaks at $d_D = 0.5$, reaching 80%, when the dealloying only happens at the surface of NPs. Due to the dealloying penetrating into the NPs and the shell expansion, the porosity of shell drops after $d_D = 0.75$, reaching 44% at $d_D = 1$.

Comparing with porous NPs from Au-core ones, Ag-core NP-precursors exhibit much larger change, including hollow

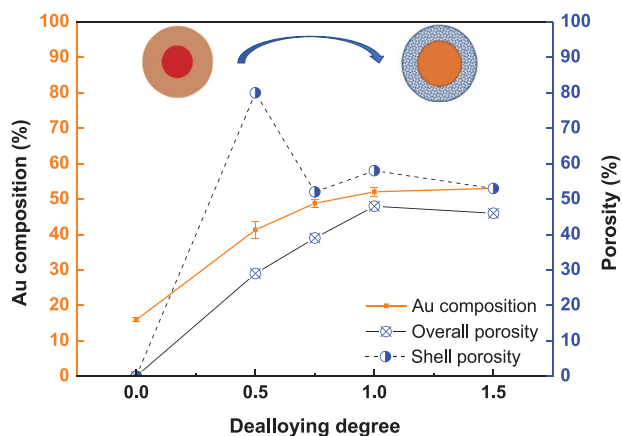


Figure 5. Effect of dealloying degree on the synthesis of porous NPs. The average porosity and Au composition of Au@Au/Ag 10/90 precursor and the NPs at dealloying degree $d_D = 0.5, 0.75, 1.0,$ and 1.5 . The value $d_D = 0$ is for the NPs precursor with 0 porosity. The schematics represent the size of core and exterior shell before and after dealloying.

interior, and plasmonic peaks of porous nanoshells shift to NIR region. To investigate the influence of d_D on Ag@AuAg precursor NPs, we performed GRR on 70 nm Ag core and alloy shell of Au/Ag 25/75 with $d_D = 0.5, 1.0,$ and 1.5 . Due to the large amount of Ag existing in the precursors, more dealloying agent (HAuCl_4) is required, thus greatly affecting the structure. The extinction spectra and TEM reveal the spectral and structural changes in dealloying process (Figure 6). The inserted photo in Figure 6a shows the color of NP dispersion change from orange to blue and pale blue-gray. Based on the extinction spectra and TEM images, the surface of NPs roughens, and the interior begins to hollow at the early stage ($d_D = 0.5$), resulting in a significant redshift from 509 to 730 nm. With higher d_D , at 1.0, the NPs become porous nanoshells with hollow interior, and the plasmonic peak shifts further, up to NIR region. With an excess of HAuCl_4 , at $d_D = 1.5$, the porous shell enlarges in different ways, the surface of the porous shells grows into large crowns or becomes thicker and solid. The extinction peak does not shift significantly compared to $d_D = 1.0$, which implies that the hollow interior remains intact.

Detailed statistics on the size of core and shell, composition as well as overall porosity has been listed in Table S2 (Supporting Information). The size of porous NPs enlarges at $d_D = 0.5$, which indicates that the dealloying takes place near the surface, so that the deposition of Au appears on the surface, as the pores also begin to form locally. At $d_D = 1.0$, with more removal, the pores integrate into hollow interior, and NPs transform into porous shells. Meanwhile, the size of shell slightly shrinks, which can be the results of micro collapse during large scale removal of Ag as well as the Au deposition onto the internal frontier. From d_D of 1.0–1.5, the shell enlarges while the hollow interior expands slightly as well. The removal of Ag continues while more Au grows onto the surface of NP, which is in accordance with the TEM images showing a big crown or thick shell formation.

Due to the vast and fast dealloying, dealloyed NPs from Ag-core precursors exhibit larger variation, including the size of hollow interior and porous shell. Meanwhile, the overall porosity of porous shell is increasing with d_D , caused by the size enlargement at higher d_D . At $d_D = 1.0$, the distribution is still similar with the Au-core NP-precursors, showing finely controlled structure. Considering both porosity and dispersity, porous nanoshells at $d_D = 1.0$ offers high potential by demonstrating both high porosity and uniform structures.

Dealloying degree easily adjusts the reaction extent through controlling the amount of added HAuCl_4 . Dealloying near the surface increases the shell diameter, while the further dealloying inside NPs fine-tunes the structure, thus the optical properties. The d_D combined with the design of core-shell structure in precursor finely control the tailoring of final porous NPs.

Composition of precursors significantly affects the dealloying kinetics, due to the high reactivity of Ag and inertness of Au. Controlling the composition distribution of precursors will therefore regulate the structural, compositional, thus optical properties of final porous NPs. We employed precursors of different compositions and investigated its effect on the resulted structure after dealloying. Based on the established study on Au–Ag alloy, there exists a critical electrochemical potential for the onset of percolation dealloying, which is dependent on the composition, and the composition bound of AuAg alloy is at least $\approx 55\%$ Ag.^[24]

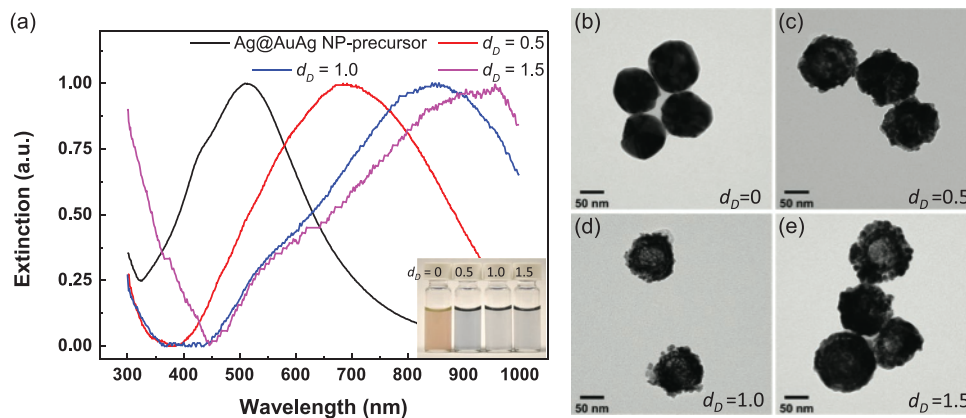


Figure 6. Effect of dealloying degree on the synthesis of porous nanoshells. a) Extinction spectra and b–e) TEM image of Ag@Au/Ag precursor and NPs after GRR with d_D of 0.5, 1.0, and 1.5.

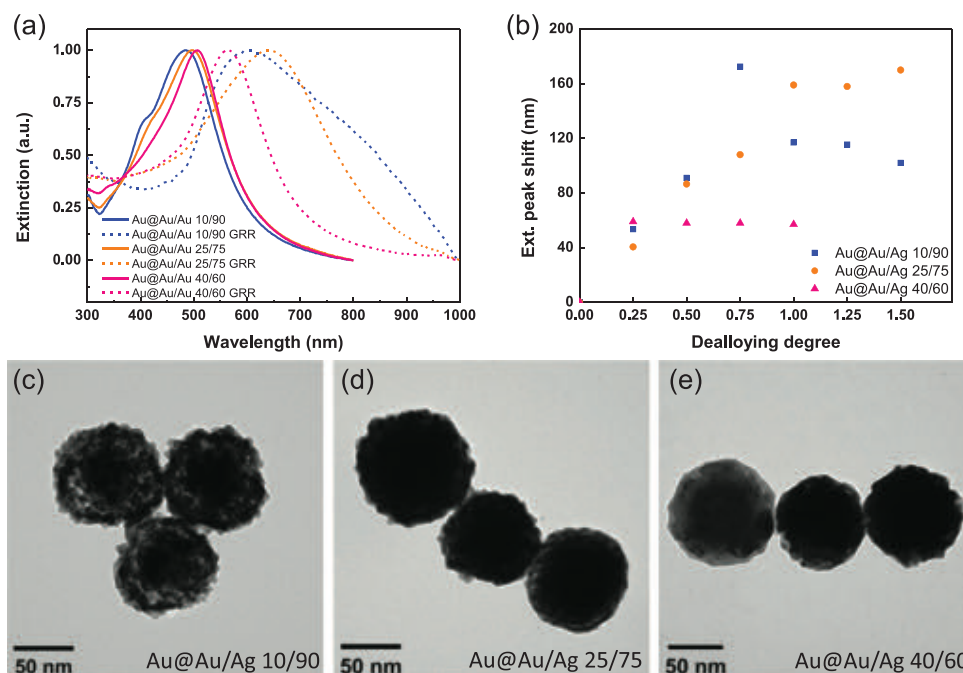


Figure 7. Effect of shell composition on the synthesis of porous NPs. a) Spectra of Au@Au/Ag NPs with shell composition of Au/Ag 10/90, 25/75, and 40/60, three kinds of precursor NPs before and after GRR ($d_D = 1.0$). b) The extinction shift of Au/Ag 10/90 (blue square), Au/Ag 25/75 (orange circle), and Au/Ag 40/60 (pink triangle) with different d_D in GRR. c–e) TEM images of NPs at $d_D = 1.0$ from precursors with shell composition of Au/Ag 10/90, 25/75, and 40/60.

We used Au@Au/Ag precursors composed of an alloy shell with composition of Au/Ag 10/90, 25/75, and 40/60, with 40 nm Au core located at the center. **Figure 7a** shows the extinction spectra of the three kinds of NP-precursors of similar size (≈ 90 nm) with shell composition of Au/Ag 10/90, 25/75, and 40/60, before and after d_D of 1.0. Extinction peaks broaden and show recognizable redshift after dealloying. Some of dealloyed NPs show asymmetry, a usual signature of NPs composed of a core and a shell or heterogeneous in composition. Especially, dealloyed NPs from Au/Ag 10/90 showed broad extinction peak due to the inhomogeneous structure. **Figure 7b** shows the extinction peak shift of NPs at different d_D . Au@Au/Ag 10/90 NP-precursors (blue squares) exhibit the largest shift (over 170 nm) at $d_D = 0.75$, while the porous structure collapses or the porosity reduces at $d_D > 1.0$, with plasmon peak shifting back. Au@Au/Ag 25/75 NP-precursors (orange circles) induce gradual peak shift within a wide d_D range (up to 1.0), and demonstrate large overall shift, reaching up to 160 nm. After the almost linear shift, the peak position becomes stable after $d_D = 1.0$, and the further deposition of Au leads to small redshift at $d_D = 1.5$. Au@Au/Ag 40/60 NP-precursors (pink triangles) yield relatively small peak shift (≈ 60 nm) during the early stage of GRR, while there is almost no change when $d_D > 0.25$.

To directly compare the structure of dealloyed NPs from different compositions, we also analyzed the NPs at the same $d_D = 1.0$ with TEM. **Figure 7c–e** shows the dealloyed NPs from Au@Au/Ag precursors with shell composition of 10/90, 25/75, and 40/60, respectively. The structure of surface and pores vary significantly with the composition. The dealloyed NPs from Au@Au/Ag 10/90 NP-precursors appear as porous shells with rough surface and the spongy interior surrounding the left

core. However, the NPs dealloyed from Au@Au/Ag 25/75 precursors exhibit clear pits and holes near the surface, forming a separation of core and shell. Moreover, the Au@Au/Ag 40/60 NPs are only slightly dealloyed at the surface, and the loss of atoms formed pits and roughened the surface, limited by the composition of 40% Au. Thus, by adjusting the composition of precursors, we produced three different structures. The plasmonic peak shifts shown in **Figure 7a** are clearly explained by the presence of pores or hollowness formed in the interior and pits with roughness of the surface.

In bulk Au–Ag dealloying, there exist composition-dependent critical potential, which decreases with higher Ag composition.^[24a,b,25] With lower critical potential, the precursor is more susceptible to dealloying. Applied in NPs under GRR, the controlled composition of the NP-precursors efficiently adjusts the removal of Ag atoms and deposition of Au atoms. The precursors with composition close to critical composition for dealloying, are limited by the compositional threshold, which means only a small number of Ag atoms can be removed until reaching the critical composition, GRR resulting in limited change of the surface roughness. Faster and more intense dealloying occurs with Ag-rich precursors, resulting in rough surfaces with higher curvature and more removal of Ag atoms and vacancies formed in the NPs as dealloying penetrates the interior of NPs. The final size, composition and the gap between core and shell are strongly dependent on the easily tunable composition of precursors, which makes the dealloyed structure predictable and enables the specific structure design. When combining with d_D , the design of the porous structure and optical properties of the dealloyed NPs can be more flexible by tuning the dimension and morphology of the core and shell.

Compositional effect not only influences the GRR process on Au-core precursors, but also on Ag-core ones. Note that it is difficult to dealloy deeper layers of the Au/Ag 40/60 shell with GRR, where only the surface layer (<10 nm) are affected, exhibiting bumps and roughness for Au@AuAg NP-precursors. We opted to investigate the dealloying of pure Ag and Ag@Au/Ag 10/90 and Au/Ag 25/75 core-shell NPs. GRR transforms the precursors into hollow shells with different shell thicknesses and porosities. Pure Ag precursors tend to result in uniform shells, which has been widely observed before with nanocubes or nanospheres for nanocages, nanoboxes and nanoshells.^[13a,26] The homogeneous Au deposition in dealloying forms a thin but smooth layer on the surface of pure Ag. Only after the whole hollowing process, the alloyed shell can generate several pinholes on the surface. However, the alloy-shell precursors provide intrinsic “heterogeneous” structure with discontinuity of either Ag or Au, which creates numbers of pits and interrupts the continuous deposition over the surface during dealloying. Au islands and untouched Ag affix to each other, and their realloying occurs simultaneously with the hollowing. Rough surface and porous structure with penetrable shell are realized with the alloy shell, and the adjustable dimension of core-shell structure facilitates the size tuning in terms of hollow interior as well as the shell thickness.

2.4. Single NP In Situ Spectral Characterization

In situ study on dealloying of plasmonic NPs has been performed to deeply understand the nanostructure evolution.^[12e,27] Many researchers have used the state-of-the-art spectroscopic and microscopic equipment in the study, such as in situ optical spectroscopy and in situ TEM. Our recent published work on electrochemical etching of AuAg alloys NPs employed highly specialized in situ TEM for directly observing the nanostructure during the dealloying.^[28] In this work, we combined the more accessible optical spectrometer with back-reflection mode microscopy (Figure 8a) to enable real-time monitoring the scattering spectra of individual NPs during the dealloying process.^[29]

Similar as dealloying in colloidal, the spectra of individual NPs also exhibit redshifting and broadening, while significant differences in details are observed among the individual NPs. Scattering spectra before and after dealloying (Figure 8b) are collected from identical Au@AuAg NPs with 40 nm core and shell position of Au/Ag 25/75, and the peak position and intensity (Figure 8c) are tracked in real-time detection. Figure 8b clearly demonstrates that the peak has redshifted accompanied with broadening. Figure 8c shows the real-time change, including peak position and intensity, after the addition of H₂AuCl₄. At first, peak position stabilizes around 558 nm and after 3 min, at the position of the arrow as the reaction begins, the peak has abruptly redshifted (for around 25 nm), indicating that the fast dealloying has occurred. The early stage redshift observed from every NP during the GRR probably comes from the surface pitting, gap forming between core and shell, compositional change as well as the surrounding of high-refractive index of AgCl (2.06 compared with 1.33 of water).^[26b,30] The effect of AgCl as surrounding media has not been considered in the colloidal dealloying since the amount is relatively small, especially after certain times of washing, AgCl has been essentially removed from the NPs. However, in these single NP experiments, the diffusion along with dissolution of AgCl is limited with NPs immobilized on the glass compared to the ones in vigorous stirring. After an abrupt redshift, some NPs continue this red shifting until the end. However, some spectra as depicted in Figure 8c, show a small (<10 nm) blueshift, which can be caused by the realloying of the deposited Au surface with interior, and phase separation at the surface of NPs with AgCl due to further dealloying.^[27] After stabilizing, further dealloying resumes the redshifting. After the yolk-porous shell structure has formed, dealloying effect on peak shifting slows down compared with the early stage. During the dealloying, amplitude of the peak keeps decreasing until the late stage of slow redshift.

Results from individual NPs push-broom scan and real-time monitoring are in agreement with the colloidal ones. During the dealloying process, we can clearly see the single NPs scattering color change and intensity vanishing through

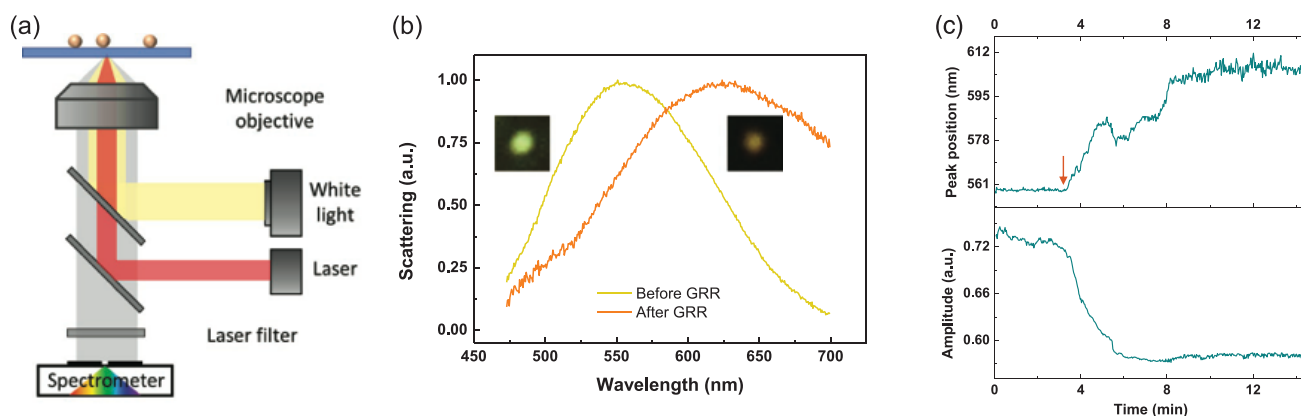


Figure 8. a) Optical setup of single NP scattering and Raman detection, combination of back-reflection mode microscope and optical spectrometer. b) Typical single NPs scattering spectra of a 40 nm Au@Au/Ag 25/75 NP before and after GRR for 30 min, inserted with the optical images and c) in situ monitoring of a scattering peak shift and intensity change during the GRR, and the arrow indicates when the reaction begins.

the microscope. From push-broom scan, the scattering spectra from many different NPs vary from each other (Figure S5, Supporting Information), but exhibit similar trends of redshift and intensity decrease. The single-NP level of observation provides more details of the evolution through GRR, moreover, real-time monitoring allows us to explore the dynamics of the process.

2.5. Application: Single-Particle SERS Monitoring

The porous plasmonic structures present a robust LSPR coupling as well as a potentially high hot spots density. Due to the crevices and rough surface, porous plasmonic nanostructures are expected to provide a promising SERS probe with high enhancement factor, enabling chemical detection with molecules at very low concentration. Porous arrays and porous single particle as SERS substrates were designed with high sensitivity.^[4c,31] As the anticancer drug doxorubicin (DOX) has poor solubility in water, and the typical drug detection is in a range of 50–5000 ng with blood plasma extraction,^[32] we propose to perform SERS on the DOX loaded porous NPs to detect and monitor the drug release. This proof-of-principle has been performed on single-particle SERS monitoring, where DOX represents both the drug and the Raman reporter. The optical setup is the same as the one in single-particle spectral study, shown in Figure 8a, and the scattering of porous NPs is employed to confirm the position of individual NPs. **Figure 9a** shows 3D-surface plot based on the images taken with the microscope under back-reflection mode (Figure S5, Supporting Information). For SERS measurement, the wavelength of irradiation laser is 633 nm and the Raman bands observed in SERS spectra are assigned accordingly (Table S3, Supporting

Information). We monitored the intensity of the most intense Raman characteristic peaks from DOX at 1244 cm⁻¹, assigned to O–H vibration.^[33] The enhancement from single NPs is therefore compared between Au NP-DOX and porous NP-DOX (Figure 9b), which are dispersed onto the glass bottom of Petri dishes. Both types of NPs are around 100 nm. The porous NP is dealloyed from Au@AuAg, whose plasmon peak is closer to the irradiation wavelength of 633 nm. The Petri dishes are filled with water, and the control signal is taken from where there is no NPs. No detectable Raman signal performed on substrate is observed while with Au-NP-DOX a very weak or even noise-level signal is detected. Note that the average field enhancement is calculated by using Mie theory to 3.9 at 633 nm from a 100 nm Au-NP leading to an estimated Raman enhancement of (3.9)⁴ or 225 (as shown in Figure S6 in the Supporting Information). The SERS signal collected from each single porous NP is intense in contrast to the very weak peak from a single Au NP. The signal collected from a porous NP can reach up to 68-fold higher than the one from a Au NP, much higher than the reported results (Table S4, Supporting Information),^[4c,34] which suggests the extremely high enhancement from our porous NPs and proves the highly sensitive detection at single-particle level. The much higher enhancement compared with standard Au NPs can be explained by a high density of hot spots from the porous structure, more loaded drug molecules (by a factor of 2, see the next section), and the Ag component which usually results from a higher Raman activity. As a rough estimation, the field enhancement of our porous nanostructure compared to Au NP is on the average (68/2)^{1/4} or 2.41, yielding to an approximate field enhancement of 3.9 × 2.41 = 9.4 and to a Raman enhancement factor of approximately (3.9 × 2.41)⁴ or 7804. We also calculated the enhancement factor by comparing

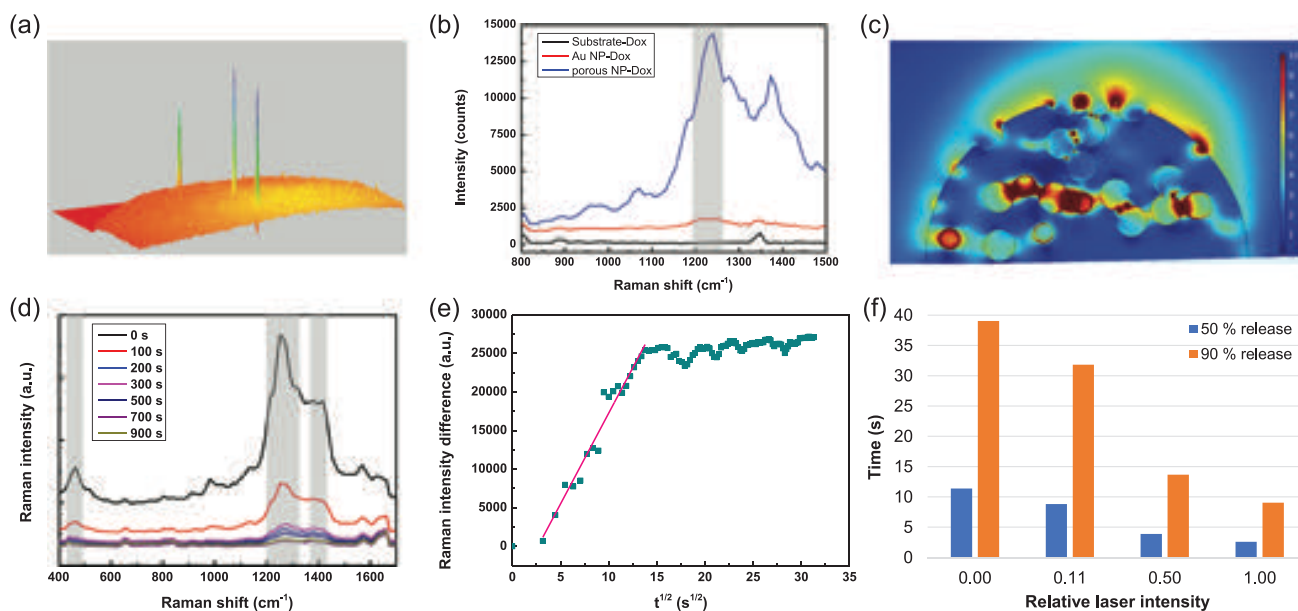


Figure 9. a) 3D-surface plot of individual porous NPs scattering observed by back-reflection mode microscopy. b) Raman signals from glass substrate, DOX-loaded single 100 nm Au NP and 96 nm porous NP deposited on the glass substrate. c) The simulated local field enhancement of porous NP under the irradiation of 633 nm laser. d) SERS spectra obtained from DOX-loaded porous Au–Ag NPs with a focused laser after the irradiation time, e) the intensity at the peak around 1250 cm⁻¹ decays in 1000 s at a step of 10 s over the square root of time and f) the time of 50% and 90% DOX release under different laser intensity (The relative value of 1.0 correspond to 7.7 × 10⁴ W cm⁻²).

the experimental Raman signal from single porous NP with the one from DOX solution (10^{-3} mol L $^{-1}$) and the estimated enhancement factor is 3866 (see the Supporting information).

To investigate the electromagnetic properties of porous NPs, the scattering field enhancement was simulated by using a finite element method (Figure 9c). The geometry of the porous structure was created by generating random holes from the surface to the solid core and controlling the porosity and the dimension of core, shell and the holes (one example shown in Figure S7 in the Supporting Information). Figure 9c shows the simulated results of the local field enhancement of a nanostructure having a 30% porosity and 100 nm diameter with 30 nm solid core, which is close to the porous NP dealloyed from Au@AuAg NP-precursor. Hot spots with field enhancement values ranging from 8 to 10 may lead to an estimated Raman enhancement factor between 4000 and 10 000 in agreement with experimental estimations.

2.6. Application: Drug Loading

The anticancer DOX is used as the drug model. To load the drug into the nanostructures, the aqueous dispersion of NPs and DOX mixture is under shaking at room temperature overnight. DOX has a characterized absorbance peak at 480 nm, which serves as the evaluation for its concentration in the solution. The loading capacity of NPs is determined by measuring the unloaded DOX in the supernatant after centrifugation. Since NPs are stabilized with citrate, which makes the NPs negatively charged, the positively charged DOX attaches to the NPs through electrostatic interaction.^[35]

To investigate the loading capacity, we employed 100 nm Au nanospheres for comparison. The Au NPs, porous NPs and porous nanoshells of similar size and same concentration of NPs are incubated with the same amount of DOX, at low and high concentration, respectively (Table 1). At low DOX concentration (30×10^{-6} M), more than twofold loading exhibits the potential of porous structures, which provide more effective surface for the attachment of drug molecules. At high DOX concentration (90×10^{-6} M), the porous shells induced almost threefold loading capacity over the spherical NPs. The increase is contributed by not only larger specific area from the porous structure, but also less weight of each NP. The drug loading test proved that the significant Raman enhancement from porous NPs over solid Au NP is mainly contributed by the porous structure and only slightly by the loading amount. Furthermore, from the optical spectra before and after drug loading, the plasmon peaks have not really shifted, indicating that the chemical composition and porous structure have not

Table 1. Drug loading capacity of different NPs with low and high concentration of DOX solution.

DOX loading	Solid NPs [mg mg $^{-1}$]	Porous NPs [mg mg $^{-1}$]	Porous nanoshells [mg mg $^{-1}$]
Low concentration	0.17	0.37	0.43
High concentration	0.73	1.24	2.15

significantly changed and that the porous NPs are stable for drug loading.

With the single-particle level SERS from porous NP, we observed the quantitative monitoring of drug release during the laser irradiation. Three relative intense characteristic peaks are noted in Figure 9d, namely the peak near 1413 cm $^{-1}$, assigned to the ring stretch; the most intense bands from C–O and O–H in the range of 1200–1300 cm $^{-1}$, and the ones at 436 and 465 cm $^{-1}$, deformation peaks corresponding to C=O.^[32,33] The intensity of Raman signal decreases with continuous laser irradiation, and the intensity change of the peak around 1244 cm $^{-1}$ were plotted over the square root of time in Figure 9e. A clear decay indicates the release of DOX triggered by laser, which fits well with the most accepted Higuchi model,^[36] in which the released amount Q follow the equation

$$Q_t = K_H t^{1/2} \quad (7)$$

where K_H is the release constant for Higuchi model. The plot of the Raman intensity decrease as a function of $t^{1/2}$ indicates a two-stage release, one is a linear fit ($R^2 = 0.96$) at the beginning, in the first 200 s, and after the fast release that can reach >92% loaded drug, another gentle slope implies a much moderate release over $t > 200$ s. The release constant K_H is related to how the molecules are strongly bonded to the NPs and the actual porosity and pore tortuosity of the nanostructure.^[37] In our case, the used porous NP has a solid core and porous shell, containing heterogeneous pores including interconnected pores near the surface, as well as the voids that penetrated into the core. The first faster step with $K_H = 2351$ s $^{-1/2}$ probably relates to the faster diffusion of DOX from the porous structure near surface, while the long-time release with $K_H = 147$ s $^{-1/2}$ much lower diffusion rate is primarily due to the small partial of DOX loaded deep into the NPs or in some narrow porous structure which creates barriers for the DOX release. The laser-stimuli release can be explained by a thermal effect of porous Au–Ag NPs, which absorbs laser light, thus inducing a local temperature increase. The thermal effect accelerates the diffusion of DOX molecules, and stimulates their release. Figure 9f exhibits the release of DOX under different laser intensity, showing the higher intensity inducing faster drug release.

It is worth noting that the irradiation laser power density is 77×10^4 W cm $^{-2}$, and focused by a 100 \times oil objective with a spot size of 244 nm. The small spot size assures the single NP under irradiation and eliminates the collective effect from multi heating source. The temperature rise has been estimated with the simplified equation^[38]

$$\Delta T(r) = \frac{\sigma(\omega)P}{4\pi\kappa r}, \text{ for } r > \text{NPs radius} \quad (8)$$

where σ is the absorption cross section at the irradiation wavelength (633 nm), P is the power density in W m $^{-2}$, κ is the thermal conductivity of water as the surrounding medium, and r is the distance from the center of the NP. The optical cross sections of porous NPs have been simulated based on Mie theory and Bruggeman's model of effective medium approximations (Figure S8, Supporting Information). The NPs are modeled with an alloy core and a porous shell with calculated porosity (as

discussed in Section 2.3), and in this case, the $\sigma = 1.2 \times 10^4 \text{ nm}^2$, $P = 7.7 \times 10^8 \text{ W m}^{-2}$, and $\kappa(\text{water}) = 0.6 \text{ W (m K)}^{-1}$. Since the NP is 96 nm in diameter, the surface temperature is estimated to be $\Delta T (r = 48 \text{ nm}) = 25 \text{ K}$. The laser irradiation generates a thermal effect within and on the surface of the porous NP, which stimulates the DOX molecules and assists their release. Meanwhile, this moderate temperature increase is tolerable since the NPs structure up to 100–250 °C, and the DOX solution has shown no effect from temperature up to 70 °C.^[38,39] Porous NPs provide not only a drug carrier, but also an active SERS substrate at single-particle level, with highly intense enhancement effect. The high enhancement plus analytical monitoring provides large prospect in biomedical applications.

3. Conclusions

This work demonstrates a versatile method to synthesize designable porous Au–Ag nanoparticles, with rough surface, and adjustable hollowness, as promising SERS probes. Au or Ag core@Au–Ag alloy shell NPs provide monodispersed precursors and regulate GRR dealloying in colloidal to produce solid core@porous shell or porous nanoshells with hollow interior. The aqueous colloidal synthesis without polymer coating provides a promising approach for large-scale production of porous NPs with accessible surface. We characterized the morphology, composition and optical properties to understand the dealloying mechanism. Through designing the composition and its distribution in alloy precursor and adjust the parameters in GRR process, we manage to tailor the hollowness and porosity, as well as plasmonic properties of final nanoparticles. Due to the rough surface and strong LSPR coupling, porous nanoparticles possess high density of hot spots and exhibit up to 68-fold higher Raman enhancement compared to Au nanospheres at single-particle level, with estimated Raman enhancement factor reaching up to 7804. The porous plasmonic nanostructure demonstrates high loading capacity with DOX as anticancer drug model, 2–3 times increase compared to solid nanospheres. The porous Au–Ag nanoparticles provide potential multifunctional platform, as cargo carrier and SERS probe. Accommodating composition distribution of Au–Ag alloy NP-precursors in colloidal GRR dealloying enlarges the possibility of porous structure design, as well as potential applications.

4. Experimental Section

Chemicals and Materials: Gold(III) chloride trihydrate ($\text{HAuCl}_4 \cdot 3\text{H}_2\text{O}$, Sigma-Aldrich), silver nitrate (AgNO_3 , Alfa Aesar) and trisodium citrate dihydrate ($\text{Na}_3\text{C}_6\text{H}_5\text{O}_7 \cdot 2\text{H}_2\text{O}$, Alfa Aesar), doxorubicin hydrochloride (DOX, Sigma-Aldrich), 4-mercaptophenylacetic acid (4-MPAA, Sigma-Aldrich), and 70 nm silver nanoparticles (no. AGCN70, nanoComposix) were received from the indicated suppliers, and used without further purification. Deionized water used in all experiments was purified by Milli-Q water purification system (Millipore) to 18.2 M Ω resistivity.

Synthesis of NP-Precursors: Au@Au/Ag alloy core–shell precursor NPs were prepared using the previously reported optimized seeded-growth method in this work.^[16] In brief, Au seeds were firstly prepared with the Turkevich method, followed by an alloy shell growth with Au and Ag coreduction in multistages until final alloy precursors. The Turkevich method usually produces Au NPs with diameter of $\approx 15 \text{ nm}$, which are

used as seeds in the following growth stage. According to the size and composition of precursors, Au–Ag alloy growth is adjusted by the amount and ratio of HAuCl_4 and AgNO_3 in the growth stages. To adjust the size of Au core, a growth stage of pure Au is performed before the growth of alloy. To obtain Ag@Au/Ag alloy core–shell precursor NPs, Ag NPs purchased from nanoComposix were used as seeds, for further growth. Similar as Au@Au/Ag NPs, a layer of pure Ag can be grown onto seeds to adjust the size of Ag core, and finally the growth of the alloy shell is performed to achieve the precursor NPs.

Taking precursors of $\approx 90 \text{ nm}$ (in diameter) Au@Au/Ag as an example, which is composed of a 40 nm Au core and a Au/Ag 10/90 shell: 3 mL Au seeds dispersion from Turkevich method was mixed with 57 mL water while stirring in a three-neck flask in 90 °C heating bath; 540 μL $170 \times 10^{-3} \text{ M}$ sodium citrate and 270 μL $30 \times 10^{-3} \text{ M}$ HAuCl_4 solution were simultaneously added into the refluxed flask in ten steps during 1 h and then the mixture was heated up to 100 °C; after 1 h, $\approx 32 \text{ nm}$ Au NPs were synthesized. After cooling to room temperature, 31.5 mL synthesized Au NPs were left in the three-neck flask as seeds for next growth stage. Then, 28.5 mL water was added, and the mixture was heated to 90 °C under vigorous stirring. The solution of 284 μL $170 \times 10^{-3} \text{ M}$ sodium citrate and simultaneously 142 μL HAuCl_4 of $30 \times 10^{-3} \text{ M}$ were added into the refluxed flask in ten steps during 1 h, and the mixture was stirred at 100 °C. After 1 h, $\approx 40 \text{ nm}$ Au NPs were obtained, which provide the seeds for alloy shell growth. After cooling down, 6 mL synthesized Au NPs were left in the flask, and 54 mL of water was added in the flask, and the dispersion was heated up to 90 °C under vigorous stirring. Then, 540 μL $170 \times 10^{-3} \text{ M}$ sodium citrate were added in ten steps during 1 h and each step followed by 27 μL $3 \times 10^{-3} \text{ M}$ HAuCl_4 and 27 μL $30 \times 10^{-3} \text{ M}$ AgNO_3 solution added simultaneously. After adding all the solution, the mixture was refluxed at 100 °C for 1 h to complete the growth.

GRR Dealloying: Precursor NP dispersion was centrifuged at 5000g, and 80% supernatant was replaced by water to remove the excess citrate. Then the NP dispersion was threefold diluted by water. HAuCl_4 as dealloying agent was slowly injected into the precursor dispersion under vigorous stirring, at a speed of 40 mL h⁻¹. The dealloying was allowed for 30 min at room temperature, and then the porous NPs were washed with water through centrifugation at 7000g. Finally, the porous NPs are dispersed in water for further use.

Drug Loading and SERS Reporter Integration: DOX was applied as anticancer drug in the loading analysis for the prepared porous NPs. Each 1 mL NPs were incubated with certain volume (20–50 μL) of $1 \times 10^{-3} \text{ M}$ DOX solution, and shaken under dark environment for 20 h. After loading, the excess DOX supernatants were measured after centrifugation at 7000g. The unloaded DOX was measured by UV–vis spectrophotometer, quantified by the intensity at the absorbance peak of 480 nm.

Characterization: The extinction spectra of colloidal precursors and porous nanoparticles were characterized by Epoch Microplate Spectrophotometer. The size, morphology and composition were characterized by JEOL 2100 Transmission electron microscope (TEM) and Oxford energy-dispersive X-ray spectroscopy (EDS) attached to it. The TEM and the high-angle-annular-dark-field (HAADF) scanning transmission electron microscope (STEM) measurements were performed at an accelerating voltage of 200 kV. Thin carbon film coated Cu grids (Electron Microscopy Sciences) were used for sample preparation, which were dipped in NPs ethanol dispersion and air-dried. Andor Shamrock SR-750 imaging spectrophotometer combined with an invert Nikon microscope were employed in hyperspectral measuring scattering spectra from individual nanoparticles. The sample were prepared in glass-bottom petri dish (MatTek), 10 μL NPs were spread onto the bottom and 4 mL of water was added. The measurements were performed with 100 \times oil objective through backreflection mode under illumination of a Halogen lamp. Similar setup and sample preparation were used in SERS measurements, instead of the halogen lamp, a focused 633 nm laser was employed as the excitation at $5.2 \times 10^4 \text{ W cm}^{-2}$ and a beam spot size of 594 nm. A filter to cut the laser wavelength was implemented before the Andor imaging spectrophotometer, and FVB mode is applied in the measuring Andor software.

Supporting Information

Supporting Information is available from the Wiley Online Library or from the author.

Acknowledgements

This work was supported by the Natural Science and Engineering Research Council of Canada. The authors would like to thank Jean-Philippe Masse at the Center for Characterization and Microscopy of Materials (CM²) for the help with the HRTEM measurements.

Conflict of Interest

The authors declare no conflict of interest.

Data Availability Statement

Research data are not shared.

Keywords

galvanic replacement, nanoprobe, plasmonic nanostructure, porous nanoparticles, single particle, surface-enhanced Raman spectroscopy

Received: August 28, 2021

Revised: September 30, 2021

Published online:

- [1] a) S. Linic, P. Christopher, D. B. Ingram, *Nat. Mater.* **2011**, *10*, 911; b) P. K. Jain, X. H. Huang, I. H. El-Sayed, M. A. El-Sayed, *Acc. Chem. Res.* **2008**, *41*, 1578; c) J. N. Anker, W. P. Hall, O. Lyandres, N. C. Shah, J. Zhao, R. P. Van Duyne, *Nat. Mater.* **2008**, *7*, 442; d) L. Wang, M. Hasanzadeh Kafshgari, M. Meunier, *Adv. Funct. Mater.* **2020**, *30*, 2005400.
- [2] a) D. Wan, X. Xia, Y. Wang, Y. Xia, *Small* **2013**, *9*, 3111; b) M. Hu, J. Y. Chen, Z. Y. Li, L. Au, G. V. Hartland, X. D. Li, M. Marquez, Y. N. Xia, *Chem. Soc. Rev.* **2006**, *35*, 1084; c) J. Wang, J. Sun, Y. Wang, T. Chou, Q. Zhang, B. Zhang, L. Ren, H. Wang, *Adv. Funct. Mater.* **2020**, *30*, 1908825.
- [3] A. N. Koya, X. Zhu, N. Ohannesian, A. A. Yanik, A. Alabastri, R. Proietti Zaccaria, R. Krahn, W.-C. Shih, D. Garoli, *ACS Nano* **2021**, *15*, 6038.
- [4] a) W. J. Lee, E. Y. Park, D. Choi, D. Lee, J. Koo, J. G. Min, Y. Jung, S. B. Hong, K. Kim, C. Kim, S. Kim, *ACS Appl. Mater. Interfaces* **2020**, *12*, 32270; b) H. Jang, D.-H. Min, *ACS Nano* **2015**, *9*, 2696; c) K. Liu, Y. Bai, L. Zhang, Z. Yang, Q. Fan, H. Zheng, Y. Yin, C. Gao, *Nano Lett.* **2016**, *16*, 3675; d) Q. Zhang, N. Large, P. Nordlander, H. Wang, *J. Phys. Chem. Lett.* **2014**, *5*, 370.
- [5] a) M. F. Cardinal, E. V. Ende, R. A. Hackler, M. O. McNally, P. C. Stair, G. C. Schatz, R. P. Van Duyne, *Chem. Soc. Rev.* **2017**, *46*, 3886; b) T. Vo-Dinh, H. N. Wang, J. Scaffidi, *J. Biophotonics* **2010**, *3*, 89; c) J. Langer, D. Jimenez de Aberasturi, J. Aizpurua, R. A. Alvarez-Puebla, B. Augu e, J. J. Baumberg, G. C. Bazan, S. E. J. Bell, A. Boisen, A. G. Brolo, J. Choo, D. Cialla-May, V. Deckert, L. Fabris, K. Faulds, F. J. Garc a de Abajo, R. Goodacre, D. Graham, A. J. Haes, C. L. Haynes, C. Huck, T. Itoh, M. K all, J. Kneipp, N. A. Kotov, H. Kuang, E. C. Le Ru, H. K. Lee, J.-F. Li, X. Y. Ling, S. A. Maier, T. Mayerh ofer, M. Moskovits, K. Murakoshi, J.-M. Nam, S. Nie, Y. Ozaki, I. Pastoriza-Santos, J. Perez-Juste, J. Popp, A. Pucci, S. Reich, B. Ren, G. C. Schatz, T. Shegai, S. Schl ucker, L.-L. Tay, K. G. Thomas, Z.-Q. Tian, R. P. Van Duyne, T. Vo-Dinh, Y. Wang, K. A. Willets, C. Xu, H. Xu, Y. Xu, Y. S. Yamamoto, B. Zhao, L. M. Liz-Marz an, *ACS Nano* **2020**, *14*, 28.
- [6] Y. Huang, W. Liu, Z. Gong, W. Wu, M. Fan, D. Wang, A. G. Brolo, *ACS Sens.* **2020**, *5*, 2933.
- [7] Y. Q. Zhang, Y. Q. Gu, J. He, B. D. Thackray, J. Ye, *Nat. Commun.* **2019**, *571*, E10.
- [8] a) N. Pazos-Perez, J. M. Fitzgerald, V. Giannini, L. Guerrini, R. A. Alvarez-Puebla, *Nanoscale Adv.* **2019**, *1*, 122; b) W.-J. Kim, S. Kim, A. R. Kim, D. J. Yoo, *Ind. Eng. Chem. Res.* **2013**, *52*, 7282.
- [9] K. Aubertin, J. Desroches, M. Jermyn, V. Q. Trinh, F. Saad, D. Trudel, F. Leblond, *Biomed. Opt. Express* **2018**, *9*, 4294.
- [10] K. Dardir, H. Wang, B. E. Martin, M. Atzampou, C. B. Brooke, L. Fabris, *J. Phys. Chem. C* **2020**, *124*, 3211.
- [11] a) J. Kim, K. Sim, S. Cha, J.-W. Oh, J.-M. Nam, *J. Raman Spectrosc.* **2021**, *52*, 375; b) J. Ma, W. Liu, Z. Ma, P. Song, Y. Zhao, F. Yang, X. Wang, *Nanoscale* **2019**, *11*, 20194; c) N. C. Lindquist, A. G. Brolo, *J. Phys. Chem. C* **2021**, *125*, 7523; d) P. Dey, T. A. Tabish, S. Mosca, F. Palombo, P. Matousek, N. Stone, *Small* **2020**, *16*, 1906780.
- [12] a) Y. Sun, B. T. Mayers, Y. Xia, *Nano Lett.* **2002**, *2*, 481; b) K. D. Gilroy, A. Ruditskiy, H. C. Peng, D. Qin, Y. N. Xia, *Chem. Rev.* **2016**, *116*, 10414; c) S. E. Skrabalak, J. Y. Chen, Y. G. Sun, X. M. Lu, L. Au, C. M. Cobley, Y. N. Xia, *Acc. Chem. Res.* **2008**, *41*, 1587; d) S. E. Skrabalak, L. Au, X. D. Li, Y. N. Xia, *Nat. Protoc.* **2007**, *2*, 2182; e) G. G. Li, Z. Wang, H. Wang, *ChemNanoMat* **2020**, *6*, 998.
- [13] a) X. Xia, Y. Wang, A. Ruditskiy, Y. Xia, *Adv. Mater.* **2013**, *25*, 6313; b) J. G. Smith, Q. Yang, P. K. Jain, *Angew. Chem., Int. Ed.* **2014**, *53*, 2867; c) J. G. Smith, X. Zhang, P. K. Jain, *J. Mater. Chem. A* **2017**, *5*, 11940.
- [14] a) W. Zhang, J. Yang, X. Lu, *ACS Nano* **2012**, *6*, 7397; b) H. Liu, K. Liu, P. Zhong, J. Qi, J. Bian, Q. Fan, K. Ren, H. Zheng, L. Han, Y. Yin, C. Gao, *Chem. Mater.* **2018**, *30*, 7744.
- [15] a) T. Zheng, G. G. Li, F. Zhou, R. Wu, J.-J. Zhu, H. Wang, *Adv. Mater.* **2016**, *28*, 8218; b) C. Zhu, D. Du, A. Eychm uller, Y. Lin, *Chem. Rev.* **2015**, *115*, 8896.
- [16] a) D. Rioux, M. Meunier, Google Patents, **2016**; b) D. Rioux, M. Meunier, *J. Phys. Chem. C* **2015**, *119*, 13160; c) L. Wang, C. Darvot, J. Zapata-Farfan, S. Patskovsky, D. Trudel, M. Meunier, *J. Biophotonics* **2019**, *12*, 201900166.
- [17] S. W. Chee, S. F. Tan, Z. Baraissov, M. Bosman, U. Mirsaidov, *Nat. Commun.* **2017**, *8*, 1224.
- [18] S. W. Chee, Z. M. Wong, Z. Baraissov, S. F. Tan, T. L. Tan, U. Mirsaidov, *Nat. Commun.* **2019**, *10*, 2831.
- [19] H. Wang, N. J. Halas, *Adv. Mater.* **2008**, *20*, 820.
- [20] a) D. Wang, P. Schaaf, *J. Mater. Chem.* **2012**, *22*, 5344; b) Y.-c. K. Chen-Wiegart, R. Harder, D. C. Dunand, I. McNulty, *Nanoscale* **2017**, *9*, 5686.
- [21] P. Dey, S. Zhu, K. J. Thurecht, P. M. Fredericks, I. Blakey, *J. Mater. Chem. B* **2014**, *2*, 2827.
- [22] Y. Sun, Y. Xia, *Nano Lett.* **2003**, *3*, 1569.
- [23] M. Hu, H. Petrova, A. R. Sekkinen, J. Chen, J. M. McLellan, Z.-Y. Li, M. Marquez, X. Li, Y. Xia, G. V. Hartland, *J. Phys. Chem. B* **2006**, *110*, 19923.
- [24] a) K. Sieradzki, N. Dimitrov, D. Movrin, C. McCall, N. Vasiljevic, J. Erlebacher, *J. Electrochem. Soc.* **2002**, *149*, B370; b) J. Erlebacher, *J. Electrochem. Soc.* **2004**, *151*, C614; c) L. Burr, I. Schubert, W. Sigle, C. Trautmann, M. E. Toimil-Molares, *J. Phys. Chem. C* **2015**, *119*, 20949; d) G. G. Li, H. Wang, *ChemNanoMat* **2018**, *4*, 897.
- [25] a) D. Artymowicz, R. Newman, J. Erlebacher, *ECS Trans.* **2019**, *3*, 499; b) J. Erlebacher, M. J. Aziz, A. Karma, N. Dimitrov, K. Sieradzki, *Nature* **2001**, *410*, 450.

- [26] a) X. Sun, J. Kim, K. D. Gilroy, J. Liu, T. A. F. König, D. Qin, *ACS Nano* **2016**, *10*, 8019; b) L. Russo, F. Merkoçi, J. Patarroyo, J. Piella, A. Merkoçi, N. G. Bastús, V. Puentes, *Chem. Mater.* **2018**, *30*, 5098.
- [27] J. G. Smith, I. Chakraborty, P. K. Jain, *Angew. Chem., Int. Ed.* **2016**, *55*, 9979.
- [28] Y. Jiang, L. Wang, M. Meunier, U. Mirsaidov, *Small* **2021**, *17*, 2006953.
- [29] S. Patskovsky, E. Bergeron, D. Rioux, M. Simard, M. Meunier, *Analyst* **2014**, *139*, 5247.
- [30] a) V. Vongsavat, B. M. Vittur, W. W. Bryan, J.-H. Kim, T. R. Lee, *ACS Appl. Mater. Interfaces* **2011**, *3*, 3616; b) A. Genç, J. Patarroyo, J. Sancho-Parramon, R. Arenal, M. Duchamp, E. E. Gonzalez, L. Henrard, N. G. Bastús, R. E. Dunin-Borkowski, V. F. Puentes, J. Arbiol, *ACS Photonics* **2016**, *3*, 770.
- [31] a) B. Chen, G. Meng, Q. Huang, Z. Huang, Q. Xu, C. Zhu, Y. Qian, Y. Ding, *ACS Appl. Mater. Interfaces* **2014**, *6*, 15667; b) M. J. Mulvihill, X. Y. Ling, J. Henzie, P. Yang, *J. Am. Chem. Soc.* **2010**, *132*, 268; c) T. Zhang, Y. Sun, L. Hang, H. Li, G. Liu, X. Zhang, X. Lyu, W. Cai, Y. Li, *ACS Appl. Mater. Interfaces* **2018**, *10*, 9792.
- [32] Z. Farhane, F. Bonnier, A. Casey, H. J. Byrne, *Analyst* **2015**, *140*, 4212.
- [33] a) H. Cao, Y. Yang, X. Chen, Z. Shao, *Nanoscale* **2016**, *8*, 6754; b) N. Strekal, A. German, G. Gachko, A. Maskevich, S. Maskevich, *J. Mol. Struct.* **2001**, 563–564, 183.
- [34] a) T. Y. Olson, A. M. Schwartzberg, C. A. Orme, C. E. Talley, B. O'Connell, J. Z. Zhang, *J. Phys. Chem. C* **2008**, *112*, 6319; b) P. Singh, T. A. F. König, A. Jaiswal, *ACS Appl. Mater. Interfaces* **2018**, *10*, 39380; c) H. Chang, Y. Y. Lee, H. E. Lee, H.-Y. Ahn, E. Ko, K. T. Nam, D. H. Jeong, *Phys. Chem. Chem. Phys.* **2019**, *21*, 9044.
- [35] a) S. Suarasan, M. Focsan, M. Potara, O. Soritau, A. Florea, D. Maniu, S. Astilean, *ACS Appl. Mater. Interfaces* **2016**, *8*, 22900; b) J. You, G. Zhang, C. Li, *ACS Nano* **2010**, *4*, 1033.
- [36] a) E. Aznar, M. D. Marcos, R. Martínez-Máñez, F. Sancenón, J. Soto, P. Amorós, C. Guillem, *J. Am. Chem. Soc.* **2009**, *131*, 6833; b) T. Higuchi, *J. Pharm. Sci.* **1961**, *50*, 874; c) W. I. Higuchi, *J. Pharm. Sci.* **1962**, *51*, 802.
- [37] M. Otsuka, H. Nakagawa, A. Ito, W. I. Higuchi, *J. Pharm. Sci.* **2010**, *99*, 286.
- [38] G. Baffou, *Thermoplasmonics: Heating Metal Nanoparticles Using Light*, Cambridge University Press, Cambridge **2017**.
- [39] J. H. Beijnen, O. A. G. J. van der Houwen, W. J. M. Underberg, *Int. J. Pharm.* **1986**, *32*, 123.